Title
Construction of a Pt-CeOx Interface for the Electrocatalytic Hydrogen Evolution Reaction

Authors
Yu, Shen-Wei
Kwon, Soonho
Chen, Yizhen
et al.

Publication Date
2024

DOI
10.1002/adfm.202402966

ADVANCED FUNCTIONAL MATERIALS
www.afm-journal.de

Construction of a Pt-CeO_x Interface for the Electrocatalytic Hydrogen Evolution Reaction

Shen-Wei Yu, Soonho Kwon, Yizhen Chen, Zhenhua Xie, Xiner Lu, Kai He, Sooyeon Hwang, Jingguang G. Chen, William A. Goddard III,* and Sen Zhang**

The creation of metal-metal oxide interfaces is an important approach to fine-tuning catalyst properties through strong interfacial interactions. This article presents the work on developing interfaces between Pt and CeO_x that improve Pt surface energetics for the hydrogen evolution reaction (HER) within an alkaline electrolyte. The Pt-CeO_x interfaces are formed by depositing size-controlled Pt nanoparticles onto a carbon support already coated with ultrathin CeO_x nanosheets. This interface structure facilitates substantial electron transfer from Pt to CeO_x, resulting in decreased hydrogen binding energies on Pt surfaces, and water dissociation for the HER, as predicted by the density functional theory (DFT) calculations. Electrochemical testing indicates that both Pt specific activity and mass activity are improved by a factor of 2 to 3 following the formation of Pt-CeO_x interfaces. This study underscores the significance and potential of harnessing robust interfacial effects to enhance electrocatalytic reactions.

1. Introduction

Deep decarbonization of the energy sector needs green hydrogen (H_2) from water electrolysis to complement renewable electricity.[1] The water electrolysis process involves two redox half-reactions: the formation of H_2 occurs at the cathode via the hydrogen evolution reaction (HER), and the production of O_2 via the oxygen evolution reaction (OER) at the anode. Both reactions require catalysts, typically precious metals, to overcome kinetic barriers and reduce overpotentials to achieve a reasonable reaction rate.[2,3] This challenge is pivotal for the widespread adoption of water electrolysis at a larger scale. An exciting advance in water electrolysis technologies in recent years is the development of alkaline exchange membrane electrolysis, which allows for the use of a diluted alkaline electrolyte, which is a major departure from the concentrated base solution used in conventional alkaline electrolyzers and the acidic environment utilized in proton exchange membrane electrolyzers.[4] Such a benign electrolyte enables utilization of earth abundant and less expensive OER catalysts (e.g., FeNiOOH and Co-based catalysts).[4–8] However, the HER becomes kinetically sluggish in alkaline electrolytes. Despite significant research efforts aimed at finding alternative, non-precious metal HER catalysts, including Ni-, Co-, Mo-, and W-based alloys, sulfides, nitrides, and phosphides as well as porphyrin and corrole complexes,[9–24] Pt- and Ru-based materials remain the most effective HER catalysts in an alkaline environment.[25,26]

While low proton concentration and the necessary water dissociation step are considered two factors limiting the HER kinetics in an alkaline electrolyte, prior investigation onto the HER activity on various monometallic surfaces revealed that it can be correlated with the calculated hydrogen binding energy (H_{BE}), which determines why Pt outperforms other monometallic surfaces for HER.[27] Moreover, theoretical studies indicated that the H_{BE} on Pt (111) is slightly stronger than the "ideal" value for the favorable HER kinetics.[28] This issue may become more pronounced when utilizing small Pt nanoparticles, a more practical form for catalysts, as they possess a greater number of low-coordination sites with higher H_{BE} values. This suggests that fine-tuning Pt surface energetics would be a promising strategy to improve both activity and cost-efficiency for the HER.

Here we report that construction of metal-metal oxide interfaces offers a viable approach to modulate Pt surface

S.-W. Yu, Y. Chen, S. Zhang
Department of Chemistry
University of Virginia
Charlottesville, VA 22904, USA
E-mail: sz3t@virginia.edu
S. Kwon, W. A. Goddard III
Materials and Process Simulation Center
California Institute of Technology
Pasadena, CA 91125, USA
E-mail: wag@caltech.edu
Z. Xie, J. G. Chen
Department of Chemical Engineering
Columbia University
New York, NY 10027, USA
E-mail: jgchen@columbia.edu
X. Lu, K. He
Department of Materials Science and Engineering
University of California
Irvine, CA 92697, USA
S. Hwang
Center for Functional Nanomaterials
Brookhaven National Laboratory
Upton, NY 11973, USA

The ORCID identification number(s) for the author(s) of this article can be found under https://doi.org/10.1002/adfm.202402966

DOI: 10.1002/adfm.202402966

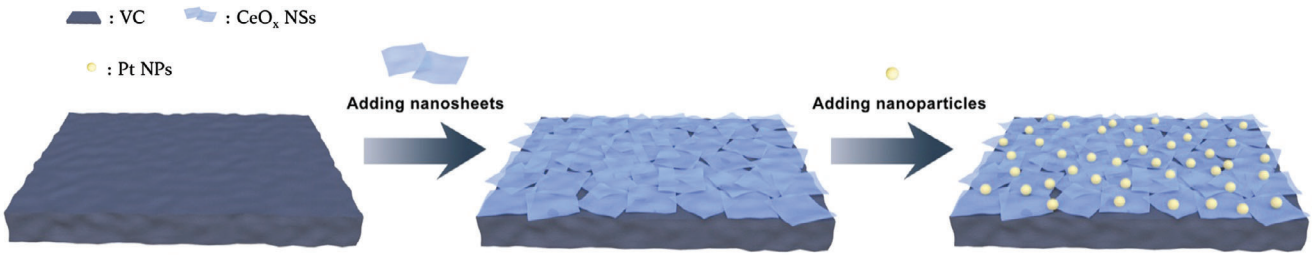

Figure 1. Schematic illustration of preparing Pt/CeO_x/C catalyst.

energetics for the HER in an alkaline environment. Metal-metal oxide interfacial interaction is a well-established concept in thermal catalysis;[29,30] however, it has received less attention in electrocatalysis. In thermal catalysis, active metal oxides such as CeO_2 and TiO_2 are known to induce electron transfer from Pt when employed as supporting materials.[31] We anticipate that HER on Pt would also benefit from such electron transfer phenomena, because the electron deficient state of Pt might result in the reduction of H_{BE} if similar active Pt-metal interfaces can be created. To verify this hypothesis, as illustrated in **Figure 1**, we load Pt nanoparticles (NPs) onto a Vulcan carbon that is precoated with ultrathin CeO_x nanosheets (NSs). The ultrathin CeO_x NSs (predominantly Ce_2O_3) is believed to serve as electron sinks, and due to their atomic-thin nature (comprising 2–4 atomic layers) and the short electron transport pathway across them, the electric conductivity of the electrocatalyst remains uncompromised. Our DFT calculations confirm the electron transfer from Pt to CeO_x when they are in direct contact, and consequently a decreased H_{BE}, which also aligns with experimental characterizations. The formation of Pt-CeO_x interfaces leads to a 2-to-3-fold improvement in both the specific activity and the mass activity of Pt, demonstrating the critical role of interfacial interactions in dictating the properties of the catalyst.

2. Results and Discussion

2.1. Catalyst Synthesis and Structural Characterization

The CeO_x NSs were prepared through the decomposition of cerium (III) acetate in benzyl ether, using oleylamine and oleic acid as surfactants (Supporting information). In a previous study, we employed a similar colloidal synthesis to make 1-D nanorods assembled by atomically precise ceria clusters, when the sole surfactant of oleic acid was used.[32] By modifying the synthesis with additional surfactant of oleylamine, we obtained 2-dimensional NSs instead of nanorods. This change in morphology is likely attributed to the strong coordinating influence of oleylamine, which stabilizes the basal plane of the NSs, leading to their preferential 2D growth. The transmission electron microscopy (TEM) image, displayed in **Figure 2a**, exhibits a cubic-like morphology of as-synthesized CeO_x with a lateral length of ≈53 nm. The TEM image in Figure 2c provides a side-view of CeO_x based on their vertical assemblies, confirming the ultra-thin nature of the CeO_x NSs (≈1.2 nm). The aberration-corrected scanning transmission electron microscopy (STEM) high-angle annular dark field (HAADF) image of CeO_x and its fast Fourier transformation (FFT) pattern indicate that the cubic lattice of Ce_2O_3 with characteristic {004} fringe (Figure 2b).[33–35]

After loading the CeO_x NSs onto Vulcan carbon (CeO_x/C), we annealed the sample in air at 200 °C to remove the organic surfactant. This annealing process is commonly employed to clean the surfactant of nanoparticles for catalysis.[36,37] As revealed by the HAADF-STEM images and the electron energy loss spectroscopy (EELS) elemental mapping (Figure 2d), the carbon support surface is uniformly coated by the CeO_x NSs, forming a thin layer of CeO_x over carbon. Additionally, the analysis conducted using X-ray photoelectron spectroscopy (XPS) indicated that a portion of the Ce_2O_3 underwent oxidation upon annealing in air. This is evident from the decrease in the Ce^{3+} ratio from 81.1% to 55.2% during the annealing process (Figure S1, Supporting Information). It is important to note that while Ce_2O_3 remains the primary component in our catalyst, the use of CeO_x here specifically denotes partial oxidation of Ce.

In parallel, the Pt NPs were synthesized by reducing platinum acetylacetonate in 1-Octadecene. Formaldehyde was added as a mild reduction agent during the synthesis, while oleylamine served as a surfactant. The size of Pt NPs can be controlled by adjusting the concentrations of metal salt and oleylamine. As displayed in TEM images in Figure S2a–c (Supporting Information), the as-synthesized Pt NPs are highly uniform and can be precisely controlled in size, with diameters of around 3, 5, and 7 nm.

To build the interface between Pt and CeO_x, we followed a process graphically portrayed in Figure 1. Generally, Pt NPs of varying sizes were loaded onto the CeO_x/C as well as pure C as control catalysts, denoting as Pt/CeO_x/C and Pt/C, respectively. A subsequent heat treatment in air was utilized to remove the ligands encapsulating the Pt NPs and facilitate the direct contact of Pt and CeO_x. As shown in the TEM image (Figure S2d, Supporting Information), Pt NPs are well-dispersed within Pt/CeO_x/C. The size and morphology of Pt within Pt/CeO_x/C are also well maintained after the thermal annealing (Figure S3, Supporting Information). Furthermore, the HAADF-STEM and EELS mapping images of Pt/CeO_x/C in **Figure 3** confirms the dispersity of Pt NPs, the well-preserved CeO_x thin layer, and the physical attachment between Pt and CeO_x.

2.2. Electrochemical Performance and Spectroscopic Analysis

We evaluated the HER performances of the Pt/CeO_x/C and Pt/C samples using a typical three-electrode system with a carbon rod counter electrode, a Hg/HgO reference electrode, and a

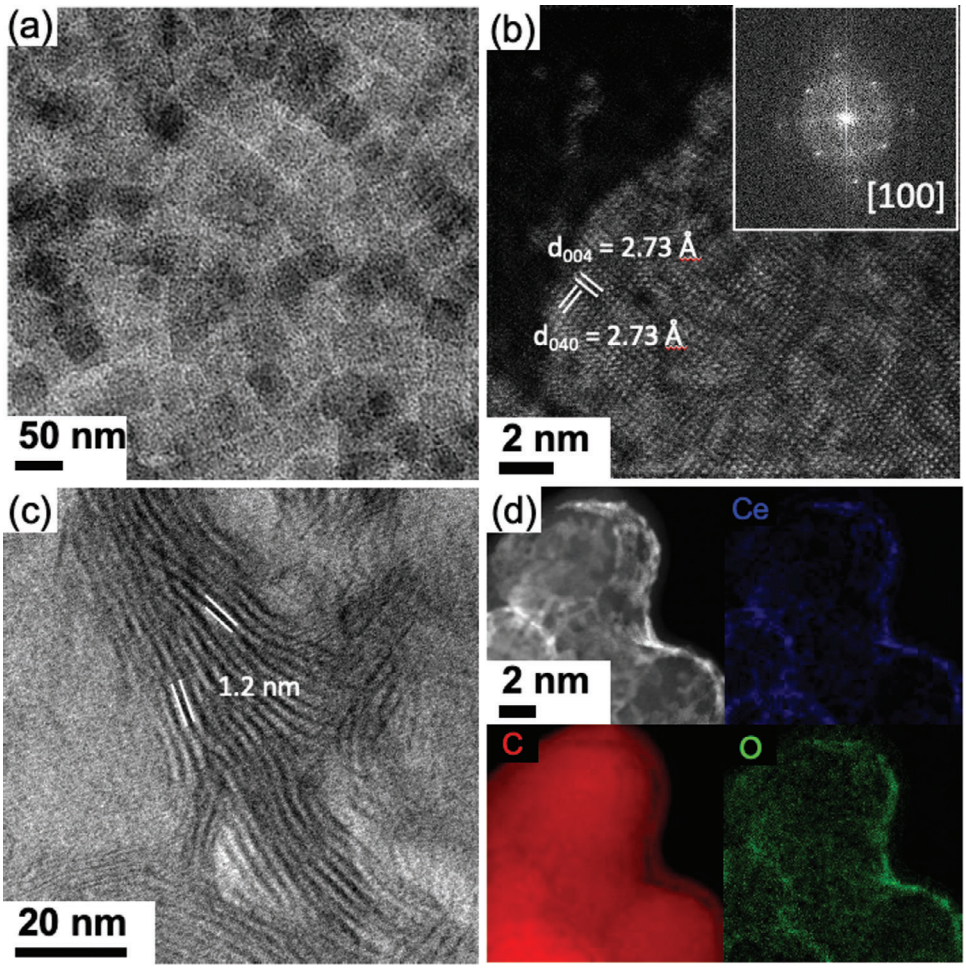

Figure 2. Morphology and structure characterizations of CeO_x NSs. a) TEM and b) HAADF-STEM images of Ce_2O_3 NSs. Inset of (b) is a FFT pattern from the whole image. c) TEM image of vertically aligned CeO_x NSs. d) HAADF-STEM and EELS mapping of the CeO_x/C support.

catalyst-loaded glassy-carbon rotating disk electrode (RDE) as working electrode. As shown in **Figure** 4a,b, the linear sweep voltammetry (LSV) curve of bare CeO_x/C, obtained in H_2-saturated 1 M KOH, exhibits negligible current density even at a very negative potential. This indicates that the electrocatalytic activity of the HER for Pt/CeO_x/C is exclusively attributed to the Pt NPs. Furthermore, it is observed that 3 nm Pt NPs present a significantly lower overpotential compared to 5 nm and 7 nm Pt NPs for both Pt/CeO_x/C and Pt/C catalysts. This could be ascribed to the larger surface area of the smaller nanoparticles. Once coupled with CeO_x, the Pt/CeO_x/C catalysts demonstrate HER activities superior to the Pt/C counterparts, regardless of Pt size, while their Pt mass loadings are consistent across different catalysts. In particular, the Pt/CeO_x/C catalyst with 3 nm Pt exhibits an overpotential of only 19 mV at 10 mA cm^{-2}. This suggests that the HER catalysis benefits from the formation of the Pt-CeO_x interfaces.

As summarized in Figure S4 and Table S1 (Supporting Information), the Pt/CeO_x/C catalyst consistently exhibits lower Tafel slopes and a higher exchange current density (j_0) compared to Pt/C with the same size of Pt. The lowest Tafel slope value of 50 mV dec^{-1} and the highest j_0 of 4.1 mA cm^{-2} are obtained on Pt/CeO_x/C with 3 nm Pt. Moreover, to assess the intrinsic activity of Pt, we obtained the electrochemical active surface area (ECSA) of Pt by analyzing the hydrogen underpotential deposition/stripping current area in the cyclic voltammetry (CVs) curves measured in a N_2-saturated 0.1 M $HClO_4$, and the results are tabulated in Figure S5 and Table S2 (Supporting Information). It is worth noting that changing supports (CeO_x/C and C) has negligible influence on Pt ECSA when the loaded Pt sizes are consistent. After normalizing the current density against ECSA, the Pt/CeO_x/C catalysts deliver the higher HER current densities than Pt/C with an enhancement factor of 2 to 3 at different overpotentials (Figure 4c), further confirming the benefit of the Pt-CeO_x interaction. As highlighted in Figure 4d and Tables S1,S2 (Supporting Information), the specific activity of Pt/CeO_x/C (3 nm Pt) reaches 2.51 mA $cm^{-2}{}_{ECSA}$ at an overpotential of 100 mV, higher than Pt/CeO_x/C (5 nm Pt) (1.94 mA $cm^{-2}{}_{ECSA}$), Pt/CeO_x/C (7 nm Pt) (1.62 mA $cm^{-2}{}_{ECSA}$), and all Pt/C catalysts.

To assess the stability of the catalysts, the chronopotentiometry (CP) method was employed at a constant current density of 100 mA cm^{-2} (Figure S6, Supporting Information). In the absence of CeO_x, the Pt/C (3 nm Pt) catalyst exhibits a rapid increase in overpotential within the first 2 hours, followed by a sustained

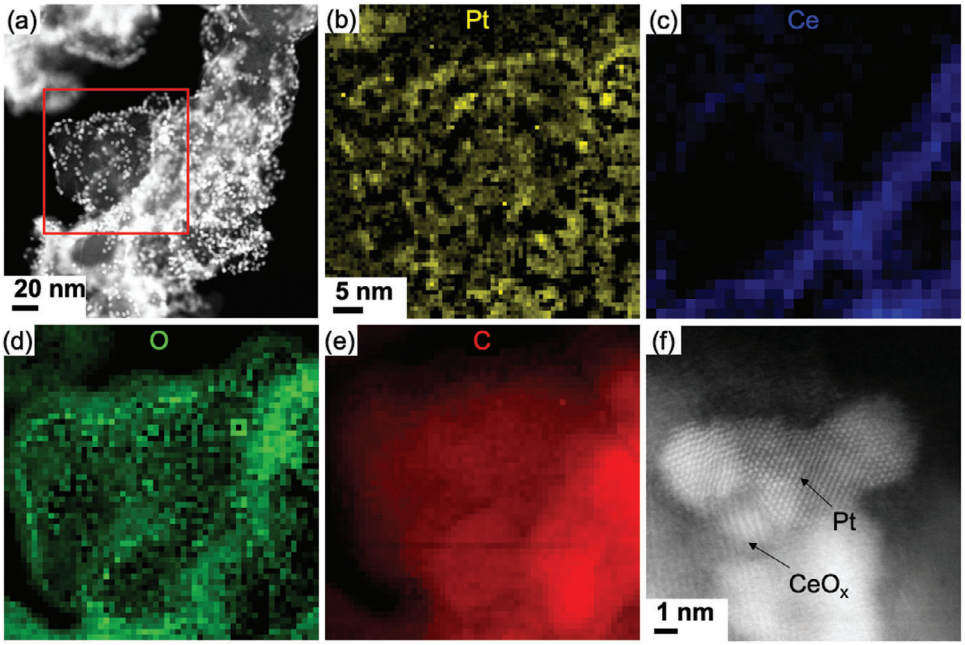

Figure 3. a) and f) HAADF-STEM images and b–e) EELS mapping of Pt/CeO_x/C (3 nm Pt) catalyst.

increase with a high deactivation rate of 129.1 mV h^{-1}. In contrast, the Pt/CeO_x/C (3 nm Pt) demonstrates an enhanced stability with a decay rate of 28.4 mV h^{-1}. Clearly, in addition to the lower overpotential and the higher activity, the Pt/CeO_x/C catalyst is better suited for prolonged electrochemical applications.

To provide more insight into electronic and atomic structures of our catalysts, in situ X-ray absorption spectroscopy (XAS) measurements were carried out at -0.1 V vs. reversible hydrogen electrode (RHE) for both Pt/CeO_x/C and Pt/C (3 nm Pt) samples. As shown in Figure 4e, the X-ray absorption near edge structure (XANES) results of both samples show broadened resonance peaks than the Pt foil, suggesting the small size of Pt NPs and the contracted distance of Pt-Pt bonds.[38,39] Furthermore, the extended X-ray absorption fine structure (EXAFS) results (Figure 4f) reveals that the average coordination number (CN) of Pt–Pt bond for Pt/CeO_x/C is 10.1 and 10.2 at -0.1 and -0.15 V versus. RHE, respectively, which are very close to the values for Pt/C under the same condition (10.5 and 10.9 at -0.1 and -0.15 V vs. RHE, respectively) (Table S3, Supporting Information). The obtained CN values correspond to Pt NPs with a size of around 3 nm assuming a hemispherical shape, and this finding is consistent with the observation from TEM and STEM images. It is important to point out that Pt/CeO_x/C and Pt/C exhibit similar oxidation states under in situ XAS experiments, both of them being metallic Pt at -0.1 V (Figure 4e,f; Figures S7,S8, Supporting Information). This suggests that their different catalytic performances under the HER condition cannot be correlated to in situ XAS result, probably due to the non-surface sensitive nature of the XAS technique.

To elucidate the Pt surface properties, CO adsorption diffuse reflectance infrared Fourier-transform spectroscopy (DRIFTS) was used to characterize the surface electron densities of Pt/CeO_x/C and Pt/C catalysts. The vibrational frequencies of adsorbed CO are sensitive to the back-donation involving *d* electrons of the metal and π^* orbitals of the CO ligand.[40,41] Thus, the frequencies of the ν_{CO} bands are good indicators of the average surface electron densities on the metal sites in heterogeneous catalysts.[40,42] The spectrum of the Pt/CeO_x/C (3 nm Pt) in Figure 4g, after CO adsorption, shows a ν_{CO} band near 2061 cm^{-1} that is assigned to linearly bound CO on Pt sites.[41] In contrast, the spectrum of Pt/C (3 nm Pt) was characterized by a ν_{CO} band with a red-shifted vibrational frequency at 2054 cm^{-1}, suggesting that the Ce_2O_3/C-supported Pt are more electron-deficient than C-supported Pt near the surface region.[43,44] Furthermore, the CeO_x/C supported Pt nanoparticles show a broader CO adsorption band with a full width at half-maximum (fwhm) of 28 cm^{-1}, higher than that on bare C supported Pt nanoparticles (fwhm = 24 cm^{-1}) and a shoulder peak located at approximately 2085 cm^{-1} was only observed on Pt/CeO_x/C (3 nm Pt), which supports the presence of Pt-CeO_x interfacial structure. This interfacial phenomenon is further validated by the DFT calculations discussed in the following section.

2.3. DFT Calculations

Cubic Ce_2O_3 has a corundum-like structure (Figure S9a, Supporting Information) containing distorted CeO_6 octahedra that result in a large unit cell, $Ce_{32}O_{48}$. Eight octahedra have six equivalent Ce—O bonds with a bond length of 2.37 Å, while the other 24 distorted octahedra have Ce—O bond lengths ranging from 2.32 to 2.46 Å. Each Ce^{3+} has an unpaired spin with all 32 Ce coupled ferromagnetically (Figure S9b, Supporting Information). Based on the experimental structure, we built a two-Ce-atom thick slab for the Ce_2O_3(100) surface (Figure S10a, Supporting Information) to serve as the substrate for deposition of Pt. In this slab, most unpaired spins are found on surface oxygen, but the coupling between the top and bottom surfaces reduces the net magnetization

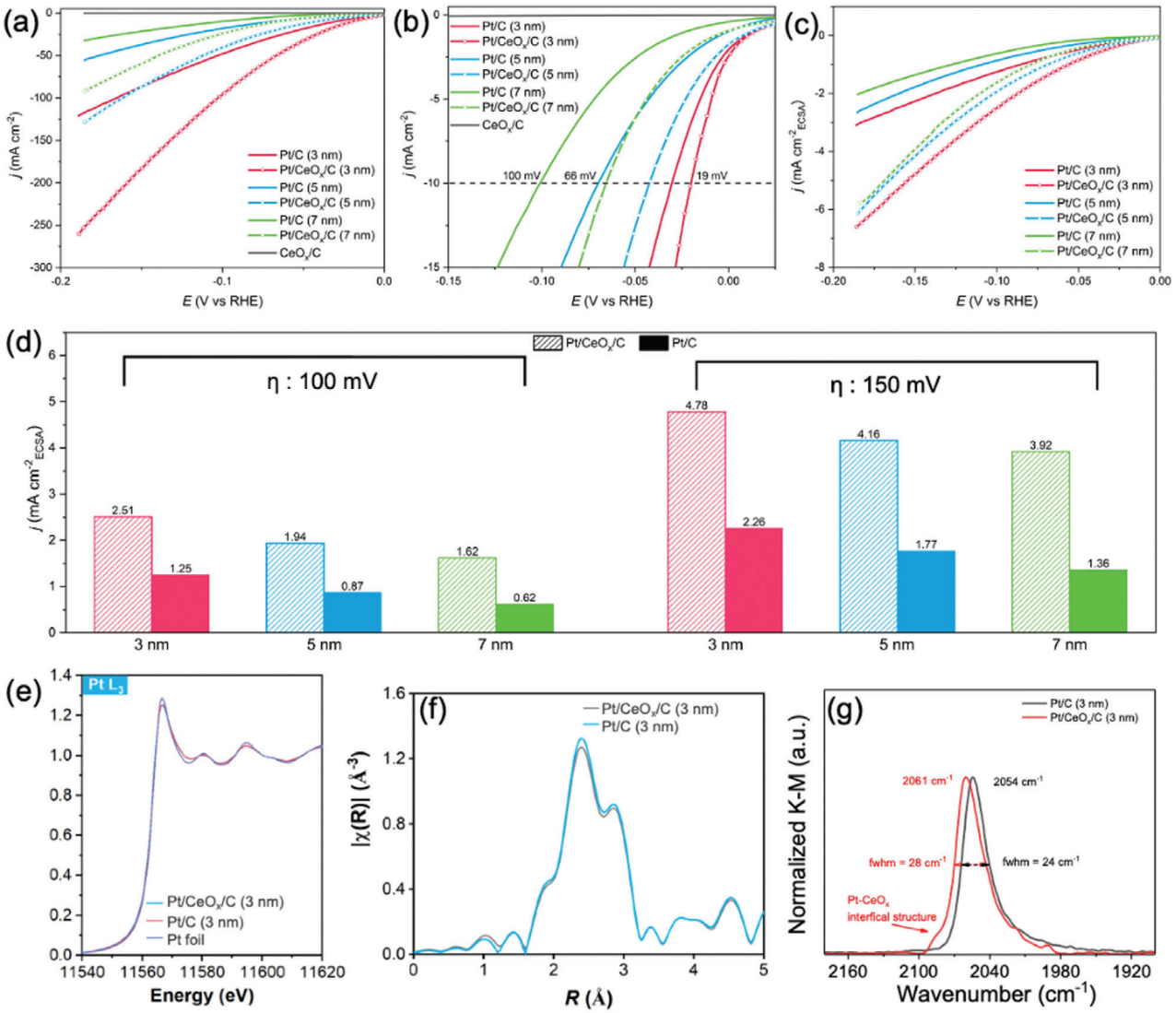

Figure 4. Alkaline HER performance, in situ XAS, and DRIFT results of different catalysts. a and b) LSV curves. c) ECSA-normalized LSVs. d) ECSA-normalized current at overpotential of 100 and 150 mV. In situ Pt L3-edge e) XANES and f) EXAFS spectra in the R space on Pt/C and Pt/CeO_x/C (3 nm Pt) catalysts at -0.1 V versus. RHE. g) CO adsorption DRIFTS in the ν_{CO} region characterizing Pt/C and Pt/CeO_x/C (3 nm Pt) catalysts. They are recorded after the samples had been in contact with flowing CO for 30 min at room temperature and a subsequent purge of the DRIFTS cell with N_2 for 60 min.

to a net spin of 6 for the whole system (Figure S10b, Supporting Information).

Although our experiments involve Pt nanoparticles with a size from 3 nm to 7 nm, we used smaller 8–10 atom Pt clusters to keep the system at a practical size for DFT calculations. Watanabe *et al.* reported exclusive formation of 2-layer Pt_n cluster for n > 9 on TiO_2(110), while the global minimum Pt_{10} cluster in vacuum has a 3-layered triangular pyramidal structure.[45–47] Our calculations show that the 2-layer Pt_{10} cluster on Ce_2O_3 (100) (Figure S11a, Supporting Information) is 3 eV lower in energy compared to the pyramidal geometry (Figure S11b, Supporting Information). For this Pt_{10} cluster structure, we found that one O climbed up onto a 3-fold site on the Pt_{10} cluster during the structure optimization. Since the oxygen is easily reduced to water at HER working conditions (Figure S12, Supporting Information), we removed this O and further minimized the Pt_{10} cluster. The final geometry is shown in **Figure 5**a. This structure does not exhibit any structural deformations during 10 ps of *ab-initio* molecular dynamics at 298 K (Figure S13 and Movie S1, Supporting Information). After binding the Pt_{10} cluster to the Ce_2O_3(100) surface, the charges redistribute, leading to an overall spin-singlet state. The Bader charge analysis[48] (Figure 5b) predicts that the Pt_{10} cluster lose 2.44 electrons to the substrate, mostly from the 1st layer as shown in Figure 5d,e.

The H_{BE} on the catalyst surface is considered as a reliable descriptor for the HER.[49] For example, DFT calculations have suggested that Pt(111) binds hydrogen slightly stronger than the optimal value for the HER.[49,50] We explored all possible 1-fold on-top, 2-fold bridge, and 3-fold hollow sites for hydrogen adsorption on Pt_{10} clusters (35 binding sites in total), as shown in Figure S14 (Supporting Information).

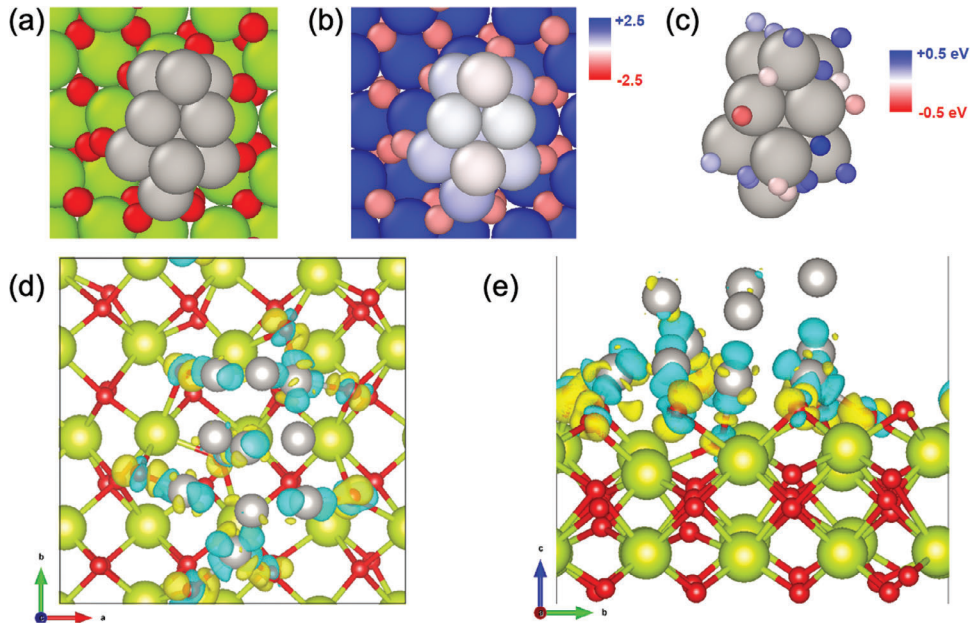

Figure 5. a) Geometric configuration of the optimized Pt_{10}/Ce_2O_3 (100) model system. Green, red, grey spheres represent Ce, O, and Pt atoms, respectively. b) Charge distribution using Bader charge analysis. Blue and red color represents net positive and negative oxidation states, respectively. c) The 18 unique H binding sites on Pt_{10}/Ce_2O_3 (100). Large grey spheres represent Pt atoms while the small spheres indicate H atom binding sites. Blue and red color represent weaker and stronger H binding, respectively, compared to that on Pt (111). d) Top and e) side view of the charge redistribution upon Pt_{10} binding on Ce_2O_3 (100). Yellow and blue isosurfaces represent charge accumulation and depletion, respectively.

During the geometry minimization, H atoms spontaneously diffuse to nearby more stable sites, leading to 18 unique sites shown in Figure 5c. The color on the H atoms represents the relative H binding energy compared to that on the Pt (111) surface (hollow site). We find that the relative binding energies vary from -0.28 to 0.47 eV with on-top sites on the 1st layer and the hollow sites between the 1st and 2nd layer being the weakest.

Clearly, the direct contact with Ce_2O_3 induces a substantial electron transfer across the interface, leading to the weakened H_{BE} found in our DFT calculations. Such decreased hydrogen adsorption is likely the reason for the enhanced HER activity in $Pt/CeO_x/C$ observed in experiment. In addition, the Pt/CeO_x interface may also facilitate the water dissociation step in the HER in an alkaline electrolyte. Previous work has reported that the incorporation of an $Ni(OH)_2$ domain on a single-crystal Pt surface allowed an improved HER kinetics because these $Ni(OH)_2$ domains enable accelerated water dissociation.[51] Given the well-established ability of water dissociation on ceria surface in thermal catalysis,[52–55] we postulated that the Pt/CeO_x interface could ease the water dissociation step for the HER, particularly in alkaline working conditions. Our DFT calculations indicate that the water dissociation energy on Pt/Ce_2O_3 (-0.76 eV) is 1 eV lower than that on Pt (111) (Figure S15, Supporting Information where the value is +0.25 eV), thereby supporting this proposed mechanism.

3. Conclusion

In summary, this study concentrated on examining the distinctive electronic structure of Pt NPs attached to ultra-thin Ce_2O_3 NSs and their impact on the performance of the HER. Our DFT calculations revealed a discernible electron transfer from Pt to the Ce_2O_3 substrates. Consequently, specific on-top and hollow Pt sites, in comparison to the unmodified Pt counterparts, displayed a desirable weakening of H_{BE}, contributing to the improved HER activity. Additionally, the Pt-Ce_2O_3 interface was found to facilitate the water dissociation step, further enhancing the HER kinetics. Experimentally, the $Pt/CeO_x/C$ catalyst exhibited enhanced HER activity compared to the Pt/C catalyst, consistent with DFT calculations. This study underscores the potential of manipulating metal-metal oxide interfaces for electrocatalytic reactions. Furthermore, we anticipate the applicability of this strategy to other domains. For instance, our CeO_x nanosheets were applied as a coating on a commercial Al_2O_3 powder support, forming a core/shell structure of Al_2O_3 materials with a thin layer of CeO_x on the surface (Figure S16, Supporting Information). This configuration can support metal NPs for thermal catalysis and extends the versatility of the approach beyond electrocatalysis.

Supporting Information

Supporting Information is available from the Wiley Online Library or from the author.

Acknowledgements

S.Y., S.K. and Y.C. contributed equally to this work. This work was supported by the U.S. Department of Energy, Office of Basic Energy Sciences, Chemical Sciences, Geosciences, and Biosciences Division (DE-SC00234430). This research used resources of the Center for Functional Nanomaterials (CFN) and beamlines 7-BM (QAS) of the National Synchrotron Light Source II (NSLS-II) at Brookhaven National Laboratory

(Contract No. DE-SC0012704 and DE-SC0012653), U.S. DOE Office of Science User Facilities. S. Z. acknowledges support from the Sloan Research Fellowship (Grant No. FG-2022-18460). S.K. acknowledges support from the Resnick Sustainability Institute at Caltech. This work used Stampede3 at Texas Advanced Computing Center through allocation DMR160114 from the Advanced Cyberinfrastructure Coordination Ecosystem: Services & Support (ACCESS) program, which is supported by National Science Foundation grants #2138259, #2138286, #2138307, #2137603, and #2138296. K.H. and X. L. acknowledge the support from the American Chemical Society Petroleum Research Fund under Grant No. 62493-DNI10, as well as the use of facilities and instrumentation at the University of California Irvine Materials Research Institute, supported in part by the National Science Foundation Materials Research Science and Engineering Center program through the University of California Irvine Center for Complex and Active Materials (DMR-2011967).

Conflict of Interest

The authors declare no conflict of interest.

Data Availability Statement

The data that support the findings of this study are available from the corresponding author upon reasonable request.

Keywords

electrolysis, hydrogen evolution reaction, metal-metal oxide interface, Pt-CeO_x

Received: February 18, 2024
Revised: April 4, 2024
Published online:

[1] D. Das, T. N. Veziroğlu, *Int. J. Hydrogen Energy* **2001**, *26*, 13.
[2] X. Cui, P. Ren, D. Deng, J. Deng, X. Bao, *Energy Environ. Sci.* **2016**, *9*, 123.
[3] R. D. L. Smith, M. S. Prévot, R. D. Fagan, Z. Zhang, P. A. Sedach, M. K. J. Siu, S. Trudel, C. P. Berlinguette, *Science* **2013**, *340*, 60.
[4] J. Xiao, A. M. Oliveira, L. Wang, Y. Zhao, T. Wang, J. Wang, B. P. Setzler, Y. Yan, *ACS Catal.* **2021**, *11*, 264.
[5] H. Zhou, F. Yu, Q. Zhu, J. Sun, F. Qin, L. Yu, J. Bao, Y. Yu, S. Chen, Z. Ren, *Energy Environ. Sci.* **2018**, *11*, 2858.
[6] F. Song, M. M. Busch, B. Lassalle-Kaiser, C.-S. Hsu, E. Petkucheva, M. Bensimon, H. M. Chen, C. Corminboeuf, X. Hu, *ACS Cent. Sci.* **2019**, *5*, 558.
[7] B. Zhang, X. Zheng, O. Voznyy, R. Comin, M. Bajdich, M. García-Melchor, L. Han, J. Xu, M. Liu, L. Zheng, F. P. García de Arquer, C. T. Dinh, F. Fan, M. Yuan, E. Yassitepe, N. Chen, T. Regier, P. Liu, Y. Li, P. De Luna, A. Janmohamed, H. L. Xin, H. Yang, A. Vojvodic, E. H. Sargent, *Science* **2016**, *352*, 333.
[8] X.-F. Lu, L.-F. Gu, J.-W. Wang, J.-X. Wu, P.-Q. Liao, G.-R. Li, *Adv. Mater.* **2017**, *29*, 1604437.
[9] A. Y. Faid, A. O. Barnett, F. Seland, S. Sunde, *Electrochim. Acta* **2020**, *361*, 137040.
[10] Z. Liang, H. S. Ahn, A. J. Bard, *J. Am. Chem. Soc.* **2017**, *139*, 4854.
[11] J. Dong, Q. Wu, C. Huang, W. Yao, Q. Xu, *J. Mater. Chem. A* **2018**, *6*, 10028.
[12] W. Hua, H.-H. Sun, F. Xu, J.-G. Wang, *Rare Met.* **2020**, *39*, 335.
[13] N. Yang, Z. Chen, D. Ding, C. Zhu, X. Gan, Y. Cui, *J. Phys. Chem. C* **2021**, *125*, 27185.
[14] J. M. V. Nsanzimana, Y. Peng, M. Miao, V. Reddu, W. Zhang, H. Wang, B. Y. Xia, X. Wang, *ACS Appl. Nano Mater.* **2018**, *1*, 1228.
[15] M. G. S. da Silva, C. M. Leite, M. A. L. Cordeiro, V. R. Mastelaro, E. R. Leite, *ACS Appl. Energy Mater.* **2020**, *3*, 9498.
[16] D. Zhang, F. Wang, W. Zhao, M. Cui, X. Fan, R. Liang, Q. Ou, S. Zhang, *Adv. Sci.* **2022**, *9*, 2202445.
[17] Y. Abghoui, E. Skúlason, *J. Phys. Chem. C* **2017**, *121*, 24036.
[18] J. Theerthagiri, S. J. Lee, A. P. Murthy, J. Madhavan, M. Y. Choi, *Curr. Opin. Solid State Mater. Sci.* **2020**, *24*, 100805.
[19] Z. Zhou, L. Wei, Y. Wang, H. E. Karahan, Z. Chen, Y. Lei, X. Chen, S. Zhai, X. Liao, Y. Chen, *J. Mater. Chem. A* **2017**, *5*, 20390.
[20] H. Du, R.-M. Kong, X. Guo, F. Qu, J. Li, *Nanoscale* **2018**, *10*, 21617.
[21] H. M. Castro-Cruz, N. A. Macías-Ruvalcaba, *Coord. Chem. Rev.* **2022**, *458*, 214430.
[22] P. Chou, L. Kim, S. M. Marzouk, R. Sun, A. C. Hartnett, D. K. Dogutan, S.-L. Zheng, D. G. Nocera, *ACS Omega* **2022**, *7*, 8988.
[23] J. Wang, Y. Gao, H. Kong, J. Kim, S. Choi, F. Ciucci, Y. Hao, S. Yang, Z. Shao, J. Lim, *Chem. Soc. Rev.* **2020**, *49*, 9154.
[24] H. J. Kim, H. Y. Kim, J. Joo, S. H. Joo, J. S. Lim, J. Lee, H. Huang, M. Shao, J. Hu, J. Y. Kim, B. J. Min, S. W. Lee, M. Kang, K. Lee, S. Choi, Y. Park, Y. Wang, J. Li, Z. Zhang, J. Ma, S.-I. Choi, *J. Mater. Chem. A* **2022**, *10*, 50.
[25] N. M. Marković, S. T. Sarraf, H. A. Gasteiger, P. N. Ross, *J. Chem. Soc., Faraday Trans.* **1996**, *92*, 3719.
[26] Q. Qin, H. Jang, X. Jiang, L. Wang, X. Wang, M. G. Kim, S. Liu, X. Liu, J. Cho, *Angew. Chem., Int. Ed.* **2024**, *63*, 202317622.
[27] W. Sheng, M. Myint, J. G. Chen, Y. Yan, *Energy Environ. Sci.* **2013**, *6*, 1509.
[28] C. G. Morales-Guio, L.-A. Stern, X. Hu, *Chem. Soc. Rev.* **2014**, *43*, 6555.
[29] I. Ro, J. Resasco, P. Christopher, *ACS Catal.* **2018**, *8*, 7368.
[30] Y. Li, Y. Zhang, K. Qian, W. Huang, *ACS Catal.* **2022**, *12*, 1268.
[31] S. M. Kozlov, K. M. Neyman, *J. Catal.* **2016**, *344*, 507.
[32] G. Johnson, M. Y. Yang, C. Liu, H. Zhou, X. Zuo, D. A. Dickie, S. Wang, W. Gao, B. Anaclet, F. A. Perras, F. Ma, C. Zeng, D. Wang, S. Bals, S. Dai, Z. Xu, G. Liu, W. A. Goddard, S. Zhang, *Nat. Synth.* **2023**, *2*, 828.
[33] C. Liu, L. Gui, J.-J. Zheng, Y.-Q. Xu, B. Song, L. Yi, Y. Jia, A. Taledaohan, Y. Wang, X. Gao, Z.-Y. Qiao, H. Wang, Z. Tang, *J. Am. Chem. Soc.* **2023**, *145*, 19086.
[34] D. Wang, Y. Kang, V. Doan-Nguyen, J. Chen, R. Küngas, N. L. Wieder, K. Bakhmutsky, R. J. Gorte, C. B. Murray, *Angew. Chem., Int. Ed.* **2011**, *50*, 4378.
[35] M. Cargnello, V. V. T. Doan-Nguyen, T. R. Gordon, R. E. Diaz, E. A. Stach, R. J. Gorte, P. Fornasiero, C. B. Murray, *Science* **2013**, *341*, 771.
[36] C. Liu, J. Qian, Y. Ye, H. Zhou, C.-J. Sun, C. Sheehan, Z. Zhang, G. Wan, Y.-S. Liu, J. Guo, S. Li, H. Shin, S. Hwang, T. B. Gunnoe, W. A. Goddard, S. Zhang, *Nat. Catal.* **2021**, *4*, 36.
[37] M. Cargnello, C. Chen, B. T. Diroll, V. V. T. Doan-Nguyen, R. J. Gorte, C. B. Murray, *J. Am. Chem. Soc.* **2015**, *137*, 6906.
[38] Y. Lei, J. Jelic, L. C. Nitsche, R. Meyer, J. Miller, *Top. Catal.* **2011**, *54*, 334.
[39] Z. Xie, H. Guo, E. Huang, Z. Mao, X. Chen, P. Liu, J. G. Chen, *ACS Catal.* **2022**, *12*, 8279.
[40] Y. Chen, H. Sun, B. C. Gates, *Small* **2021**, *17*, 2004665.
[41] T. Avanesian, S. Dai, M. J. Kale, G. W. Graham, X. Pan, P. Christopher, *J. Am. Chem. Soc.* **2017**, *139*, 4551.
[42] A. S. Hoffman, C.-Y. Fang, B. C. Gates, *J. Phys. Chem. Lett.* **2016**, *7*, 3854.
[43] D. Yang, S. O. Odoh, J. Borycz, T. C. Wang, O. K. Farha, J. T. Hupp, C. J. Cramer, L. Gagliardi, B. C. Gates, *ACS Catal.* **2016**, *6*, 235.
[44] S. Liu, W. Xu, Y. Niu, B. Zhang, L. Zheng, W. Liu, L. Li, J. Wang, *Nat. Commun.* **2019**, *10*, 5790.
[45] A. S. Chaves, G. G. Rondina, M. J. Piotrowski, P. Tereshchuk, J. L. Da Silva, *J. Phys. Chem. A* **2014**, *118*, 10813.
[46] V. Fung, D.-e. Jiang, *J. Phys. Chem. C* **2017**, *121*, 10796.

[47] I. Demiroglu, K. Yao, H. A. Hussein, R. L. Johnston, *J. Phys. Chem. C* **2017**, *121*, 10773.
[48] G. Henkelman, A. Arnaldsson, H. Jónsson, *Comput. Mater. Sci.* **2006**, *36*, 354.
[49] S. Trasatti, *J. Electroanal. Chem. Interfacial Electrochem.* **1972**, *39*, 163.
[50] J. K. Nørskov, T. Bligaard, A. Logadottir, J. R. Kitchin, J. G. Chen, S. Pandelov, U. Stimming, *J. Electrochem. Soc.* **2005**, *152*, J23.
[51] Y. Zhou, C. Sun, X. Yang, G. Zou, H. Wu, S. Xi, *Electrochem. Commun.* **2018**, *91*, 66.
[52] W. C. Chueh, C. Falter, M. Abbott, D. Scipio, P. Furler, S. M. Haile, A. Steinfeld, *Science* **2010**, *330*, 1797.
[53] D. R. Mullins, P. M. Albrecht, T.-L. Chen, F. C. Calaza, M. D. Biegalski, H. M. Christen, S. H. Overbury, *J. Phys. Chem. C* **2012**, *116*, 19419.
[54] B. Chen, Y. Ma, L. Ding, L. Xu, Z. Wu, Q. Yuan, W. Huang, *J. Phys. Chem. C* **2013**, *117*, 5800.
[55] S. Gritschneder, M. Reichling, *Nanotechnology* **2007**, *18*, 044024.